Volume 8
Number 23
21 June 2020
Pages 4965–5168

Journal of Materials Chemistry B

Materials for biology and medicine

rsc.li/materials-b

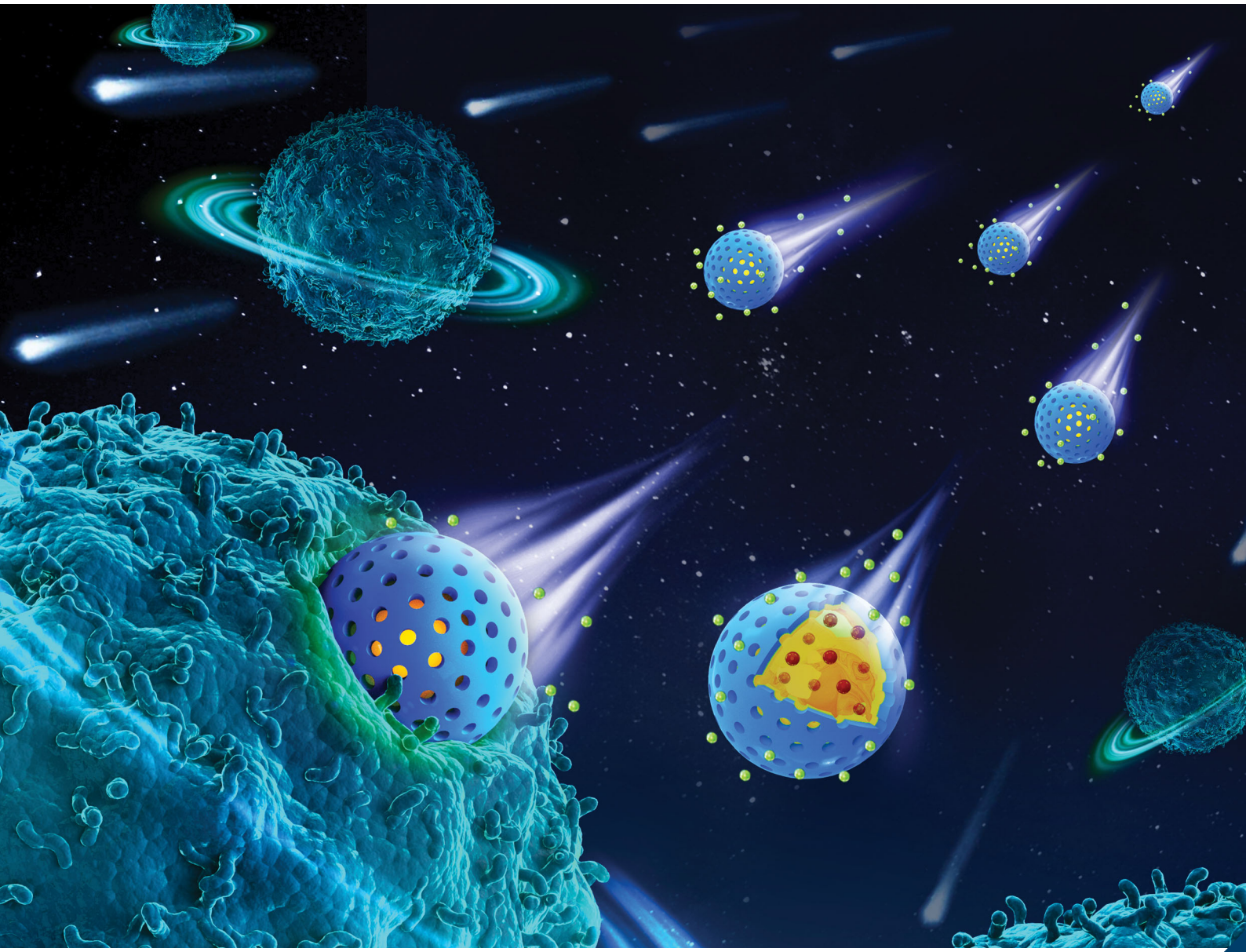

ISSN 2050-750X

ROYAL SOCIETY OF CHEMISTRY

COMMUNICATION

Xin Zhou *et al.*

Silica nanoparticle coated perfluorooctyl bromide for ultrasensitive MRI

Indexed in Medline!

Journal of Materials Chemistry B

ROYAL SOCIETY OF CHEMISTRY

COMMUNICATION

View Article Online
View Journal | View Issue

Cite this: J. Mater. Chem. B, 2020, 8, 5014

Received 21st February 2020,
Accepted 7th April 2020

DOI: 10.1039/d0tb00484g

rsc.li/materials-b

Silica nanoparticle coated perfluorooctyl bromide for ultrasensitive MRI†

Yaping Yuan,‡[ab] Qianni Guo,‡[ab] Xiaoxiao Zhang,‡[a] Weiping Jiang,[ab] Chaohui Ye[ab] and Xin Zhou *[ab]

MRI with hyperpolarized ^{129}Xe can achieve low-concentration detection. Herein, nanoparticle-coated perfluorooctyl bromide (PFOB) was developed as a ^{129}Xe MRI contrast agent with a moderate exchange rate, sufficient stability and feasible surface modification. The $\alpha_v\beta_3$ integrin overexpressed by non-small-cell lung cancer A549 cells was successfully detected by ^{129}Xe MRI with high specificity through adequate surface modifications.

Magnetic resonance imaging (MRI) is a versatile cross-sectional imaging modality with excellent penetration depth and non-ionizing radiation for opaque biological tissues.[1] Nevertheless, conventional ^{1}H MRI suffers from poor sensitivity and the influence of background signals (*e.g.* water) in the case of detecting molecules at low concentrations, such as in molecular imaging and cell labeling.[1a] To overcome these challenges, one approach is to use MRI with hyperpolarized (HP) nuclei.[2] ^{129}Xe is chemically inert and has no background signal *in vitro* and *in vivo*. The detection sensitivity of ^{129}Xe increases by four to five orders of magnitude *via* spin-exchange optical pumping techniques, resulting in the utility of MRI with low-concentration ^{129}Xe in gas and dissolved phases.[2d] HP ^{129}Xe can dissolve in tissues and blood. Several host molecules have been developed to capture ^{129}Xe atoms to realize targeted ^{129}Xe MRI.[3–7] ^{129}Xe atoms that undergo non-covalent interactions with host molecules resonate far from ^{129}Xe atoms in solution. Meanwhile, the captured ^{129}Xe atoms reversibly bind to host molecules, and they can be detected at ultralow concentration through hyperpolarized ^{129}Xe chemical exchange saturation transfer (Hyper-CEST).[8] With the advantage of Hyper-CEST, HP ^{129}Xe-based biosensors are endowed with great nuclear magnetic resonance (NMR) sensitivity and high specificity of the ligand linked to host molecules, rendering new possibilities for molecular imaging.

The typical HP ^{129}Xe biosensors were developed based on cryptophane-A that had been functionalized to bind the desired target. Such a ^{129}Xe biosensing approach has already been employed for cell labeling,[3a,b] or the detection of metal ions,[3c] pH[3d] and bio-thiols.[3e] Meanwhile, new molecular cages, such as cucurbit[*n*]uril,[4] a perfluorocarbon (PFC) nanoemulsion,[5] bacterial gas vesicles[6] or hydrophobic cavities of proteins,[7] were developed. Among all these candidates, the PFC nanoemulsion had various attractive characteristics as a ^{129}Xe MRI contrast agent because of the well-separated signal (99 ppm), high Ostwald solubility of ^{129}Xe and good biocompatibility.[5a,b] However, a high power saturation pulse was preferred to efficiently saturate ^{129}Xe in the PFC nanoemulsion because of the relatively fast exchange of ^{129}Xe,[5b] resulting in the risk of overheating in biological applications.[9] The instability of the nanoemulsion could also cause signal loss.[5b] Therefore, designing a new ^{129}Xe biosensor becomes an important but challenging issue for HP ^{129}Xe MRI.

Several factors should be considered for the rational design of a new ^{129}Xe biosensor. The capacity to accommodate multiple ^{129}Xe atoms is favourable to achieve a low detection threshold by using NMR and Hyper-CEST detection. In addition, the captured ^{129}Xe atoms should have a well-separated chemical shift from ^{129}Xe atoms in solution and experience a moderate exchange condition, which is important for efficient Hyper-CEST detection. Furthermore, the safety and stability of the biosensor under the physiological environment should be guaranteed, and the biosensor should be convenient to synthesise and modify for targeted imaging.

Mesoporous silica nanoparticles (MSNs) have served as ideal platforms for biomedical applications due to their unique chemical and physical properties.[10] MSNs have several attractive features that are well suited for a ^{129}Xe biosensor: (1) the mesopore structure can hold multiple ^{129}Xe atoms; (2) tunable pore sizes, which enable the adjustment of the exchange rate of ^{129}Xe; and (3) sufficient stability and feasible surface modification to realize

[a] *Key Laboratory of Magnetic Resonance in Biological Systems, State Key Laboratory of Magnetic Resonance and Atomic and Molecular Physics, National Center for Magnetic Resonance in Wuhan, Wuhan Institute of Physics and Mathematics, Innovation Academy of Precision Measurement Science and Technology, Chinese Academy of Sciences-Wuhan National Laboratory for Optoelectronics, Wuhan 430071, P. R. China. E-mail: xinzhou@wipm.ac.cn*

[b] *University of Chinese Academy of Sciences, Beijing, 100049, P. R. China*

† Electronic supplementary information (ESI) available. See DOI: 10.1039/d0tb00484g

‡ Y. Y., Q. G. and X. Z. contributed equally to this work.

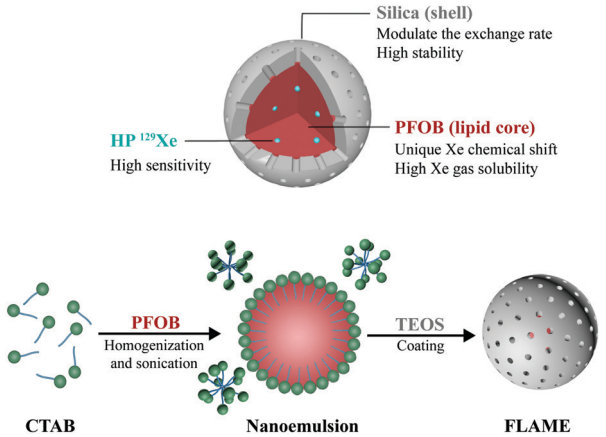

Scheme 1 Design of FLAME for ^{129}Xe MRI and synthetic scheme of FLAME. Abbreviations: CTAB, cetyltrimethylammonium bromide; TEOS, tetraethyl orthosilicate.

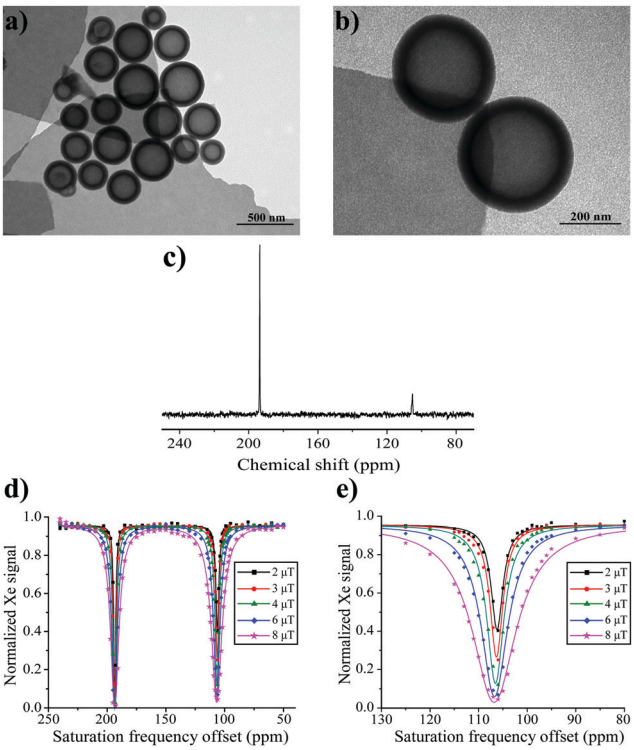

Fig. 1 (a and b) TEM image of FLAME, the liquid inner core structures are brighter than the solid outer shell. (c) ^{129}Xe NMR spectra of FLAME in PBS with four scans (pH 7.4). (d) Hyper-CEST spectra for quantitative chemical exchange saturation transfer with hyperpolarized xenon (qHyper-CEST) analysis of FLAME. (e) Zoomed-in sample of hyper-CEST spectra.

targeted imaging.[10d,e] To further improve the ^{129}Xe loading capacity of MSNs and enlarge the chemical shift difference of captured ^{129}Xe, we propose MSN coated perfluorooctyl bromide (PFOB) (also termed fluorine-accumulated silica nanoparticles for MRI enhancement [FLAME]) to host ^{129}Xe atoms with a PFOB liquid core and adjust the exchange rate with a silica shell (Scheme 1).[10a–c] PFOB, as an alternative to blood, is able to dissolve oxygen and xenon efficiently.[5a,b] The ^{129}Xe dissolved in PFOB is 10 times higher than the ^{129}Xe dissolved in water, and more importantly features a relatively long $T1$ relaxation time.[5b] Moreover, the chemical shift of ^{129}Xe in PFOB is well-separated from ^{129}Xe in water by about 90 ppm. We hypothesized that FLAME with a core–shell structure is an efficient ^{129}Xe MRI contrast agent. In this work, we characterized the NMR and Hyper-CEST signal of MSNs and FLAME. The possibility of FLAME to specifically target lung cancer A549 cells was demonstrated *via* ^{129}Xe MRI through adequate surface modification.

Firstly, we investigated the NMR characteristics of ^{129}Xe in MSNs. MSNs were synthesised *via* an emulsion template method and dispersed in PBS (pH 7.4).[11] The mesoporous structure of MSNs was observed *via* transmission electron microscopy (TEM, Fig. S1, ESI†). However, no obvious signal of ^{129}Xe@MSNs was observed in the NMR spectrum of ^{129}Xe. The Hyper-CEST technique using a selective continuous-wave (CW) saturation pulse (3.23/6.5 μT, 5 s) revealed a broad peak at 210 ppm in the Hyper-CEST spectrum, which was only 15 ppm separated from the peak of ^{129}Xe@solution (Fig. S2, ESI†). The broad peak indicated the fast exchange rate of ^{129}Xe or the inhomogeneous distribution of chemical shifts for captured ^{129}Xe atoms. However, FLAME remarkably improved the performance as a ^{129}Xe MRI contrast agent by encapsulating PFOB with a silica shell. The size distribution of FLAME was measured by transmission electron microscopy (TEM) and dynamic light scattering (DLS; Fig. S3, ESI†). The core–shell structures of FLAME were clearly observed *via* TEM images (Fig. 1a and b). FLAME was composed of a PFOB liquid core and a silica solid shell; therefore, TEM images with a light inner and dark outer are observed. The average diameter was about 325 nm for FLAME and about 250 nm for the PFOB liquid core. The N_2 adsorption/desorption isotherms of FLAME revealed a typical mesoporous structure with a pore volume of 0.63 cm^3 g^{-1} and an average pore diameter of 6.9 nm (Fig. S4, ESI†). The pores in the silica shell formed the entrance and exit channels for ^{129}Xe atoms to enter and exit from the liquid core.[10f] In this type of spherical nanoparticle, the chemical shift of the entrapped ^{129}Xe is the result of the interaction with the PFOB liquid core, and the chemical exchange of ^{129}Xe was regulated by the silica shell. Compared with the PFC nanoemulsion reported in Pines and Schröder's work,[5b,c] the exchange area in the surface of the PFOB liquid core was greatly reduced by the core–shell structures and thus slowed down the exchange of ^{129}Xe, revealing the ability of the shell to adjust the exchange rate. As shown in Fig. 1c, a unique signal at 106 ppm was obtained through four scans in the ^{129}Xe NMR spectrum. The Hyper-CEST spectra of FLAME using different saturation pulse strengths were fitted using the Lorentz function as shown in Fig. 1d and e. The Hyper-CEST signal of FLAME was quite similar to ^{129}Xe in the PFC nanoemulsion, but FLAME provided a relatively narrow, well-resolved signal. We used the qHyper-CEST method to quantify the ^{129}Xe exchange kinetics in FLAME to verify the role of the silica shell.[12] Hyper-CEST spectra with different saturation pulse strengths were fitted using the Bloch–McConnell (BM) equation in the case of HP nuclei (Fig. S5 and S6, ESI†).[12] The determined ratio of captured ^{129}Xe to free ^{129}Xe was 0.0063 (Table S1, ESI†), indicating that the concentration of FLAME is

Table 1 Characteristics of xenon hosts

Host	$\Delta\delta^a$ (ppm)	k_{ex} (s^{-1})	$N_{Xe}{}^b$	Concentration for cell labeling	NMR direct detection
FLAME	−88	131	29×10^3 [c]	nM	Yes
Cryptophane-A	−132 [d]	30 [d]	1	μM [d]	Yes
Nanoemulsion	−72 [d]	20 000 [e]	14.9×10^3 [e]	nM [d]	No

[a] $\Delta\delta$ is the relative chemical shift between Xe@solution and Xe@host. [b] N_{Xe} is the number of xenon atoms in each xenon host, which is calculated from the Ostwald solubility for PFOB (pressure = 5.45 atm, temperature = 37 °C). [c] The volume equivalent diameter of the liquid PFOB core in FLAME is about 250 nm. [d] Ref. 5*c*. [e] Ref. 5*b*.

on the picomolar scale (10^{-11} M). The determined exchange rate k_{ex} of 131 Hz was well within the slow exchange regime (Table S1, ESI†). By comparison, the chemical exchange of ^{129}Xe is on the order of 10^4 Hz for the PFC nanoemulsion and about 30 Hz for cryptophane-A in aqueous solution.[5b,c] Table 1 outlines the relevant properties of the above three xenon hosts. The fast chemical exchange of ^{129}Xe in the PFC nanoemulsion resulted in low saturation efficiency.[5b] Consequently, the Hyper-CEST contrast was inadequate unless high power saturation pulses (*e.g.*, 20 μT) were applied. The relatively slow chemical exchange of ^{129}Xe in FLAME avoided extensive line broadening and increased the spectral resolution. Low saturation pulses were also suitable for biological application due to low specific absorption rate (SAR) values.[9] These properties indicated that FLAME could be a potential ^{129}Xe nanocarrier *in vitro* and *in vivo*.

In order to explore the application of FLAME in biological systems, we carried out cell experiments after its modification. FLAME-RGD was synthesized to target $\alpha_v\beta_3$ integrin, which is overexpressed by non-small-cell lung cancer A549 cells.[13a] McF7 human breast cancer cells were selected as a negative control because this cell line expresses a low level of $\alpha_v\beta_3$ integrin.[13b,c] Dynamic light scattering (DLS) data showed a slight growth of the hydrodynamic diameter of FLAME-RGD over the course of seven days at 25° (Fig. S7, ESI†). FLAME-RGD had a zeta potential of +4.76 mV and showed low toxicity in the MTT assay (Fig. S8 and S9, ESI†). The cellular uptake of FLAME-RGD was validated *via* fluorescence imaging using confocal laser scanning microscopy (Fig. 2). The nanoparticles were internalized in A549 cells. Almost no fluorescence was observed from McF7 cells incubated with FLAME-RGD, indicating that RGD on the FLAME-RGD surface was efficient for the targeted internalization of the nanoparticles. The spot-like fluorescence image also indicated that FLAME-RGD was internalized *via* endocytosis, and nearly all nanoparticles remained in the endosomes.

The ^{129}Xe NMR spectra were obtained to confirm the FLAME-RGD uptake by cells. FLAME-RGD was incubated with a sample of 5×10^6 A549 or McF7 cells in binding buffer (containing 1% bovine serum albumin in Dulbecco's PBS) for 2 h on ice. The cells were rinsed to remove unbound FLAME-RGD and transferred into a tailored NMR tube. Hyper-CEST detection was performed as shown in Fig. 3a (sampling step, 5 ppm; saturation pulse, 6.5 μT, 5 s). As expected, a region of saturation centred at 106 ppm, characteristic of ^{129}Xe@FLAME, was observed in A549

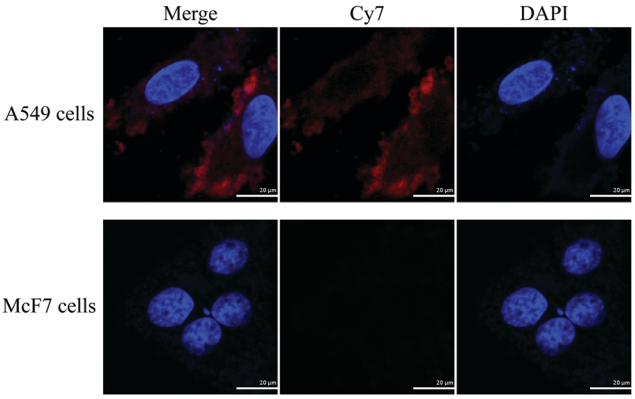

Fig. 2 Confocal laser scanning microscopy images of A549 and McF7 cells. 2×10^5 ml^{-1} A549 cells and McF7 cells were incubated for 12 h and then treated with FLAME-RGD at 0 °C for 2 h. The red fluorescence comes from the Cy7 of the FLAME-RGD, the average red fluorescence intensity was 37.97 for A549 cells and 11.12 for MCF7 cells. Measurement conditions: Cy7 was excited at 647 nm and detected at 660–760 nm. Scale bar: 20 μm.

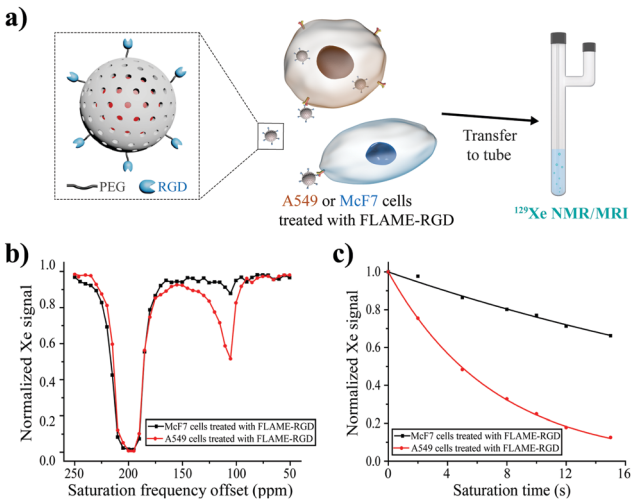

Fig. 3 NMR experiments with cell suspension samples. FLAME-RGD was incubated with A549 ($\alpha_v\beta_3$ integrin+) or McF7 ($\alpha_v\beta_3$ integrin−) cells for 2 h on ice. The cells were washed, trypsinized, resuspended in 2 ml of media and transferred to an NMR tube for NMR/MRI analysis, the final density of cells is about 2.5×10^6 cells per ml determined using a hemocytometer. (a) Schematic diagram of ^{129}Xe NMR experiments *in vitro*. (b) Hyper-CEST spectra corresponding to A549 and McF7 cell samples. The data indicated that FLAME-RGD remained in the A549 cell samples more than in the McF7 cell samples. (c) The signal depletion *versus* saturation time for A549 and McF7 cell samples.

cells (Fig. 3b, red line). The same feature was not observed with McF7 cells (Fig. 3b, black line), which established the specificity of FLAME-RGD. The effect of changing the saturation time was also measured using the same saturation pulse scheme with different saturation times (Fig. 3c). A saturation time of 2 s was sufficient to generate 24% signal depletion in A549 cell samples. Long saturation times produced additional contrast for the A549 and McF7 samples. Compared with MSNs, FLAME is much more suitable for ^{129}Xe Hyper-CEST MRI because the chemical shift of ^{129}Xe@FLAME ($\Delta\omega \approx 106$ ppm) is well-separated from

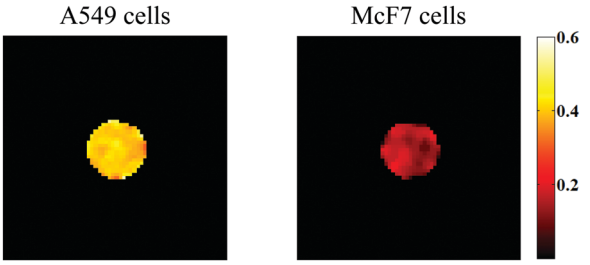

Fig. 4 ^{129}Xe Hyper-CEST MRI of A549 cells and McF7 cells treated with FLAME-RGD. The density of cells is about 2.5 × 10^6 cells per ml determined using a hemocytometer.

^{129}Xe@solution ($\Delta\omega \approx 195$ ppm), and the relatively slow chemical exchange of ^{129}Xe is highly suitable for signal assignment and a low SAR value in Hyper-CEST.

Frequency-selective Hyper-CEST MRI was performed on a 400 MHz Bruker AV400 wide-bore spectrometer to explore the potential of FLAME-RGD as a targeted ^{129}Xe MRI contrast agent. A fast spin-echo sequence was employed with a 10 s 6.5 μT CW saturation pulse after the delivery of HP ^{129}Xe into the cell samples. The saturation pulse was applied at 284 ppm for off-resonance Hyper-CEST images and 106 ppm for on-resonance Hyper-CEST images (Fig. S10, ESI†). The Hyper-CEST contrast was calculated by pixel as shown in Fig. 4. An obvious Hyper-CEST effect was generated in the A549 cell samples (mean value of 41%), and low contrast appeared in the McF7 cell samples (mean value of 15%). This result demonstrated that receptor-mediated endocytosis greatly increased the internalization of FLAME-RGD and enhanced the Hyper-CEST contrast. FLAME can indeed report biologically relevant levels of a specific biomarker as a multimodal probe for Hyper-CEST MRI and fluorescence imaging.

We demonstrated that FLAME displayed excellent Hyper-CEST MRI properties, including a suitable exchange rate and large chemical shift from ^{129}Xe@solution. Although the PFC nanoemulsion had established potential biological application, the lack of stability and impractical surface modifiability are still unsolved problems; moreover, the relatively fast exchange rate is still limiting the application of a saturation pulse and reduces the spectral resolution and contrast.[5a] The residence time of xenon atoms in the PFC nanoemulsion mainly depends on the diameter of the droplets, the diffusion coefficient of xenon in PFC and the escape probability when xenon atoms reach the boundary of the nanoemulsion.[5a] In FLAME, the core–shell structures greatly reduce the surface exchange area of the PFOB liquid core and decrease the escape probability of xenon atoms. The core–shell structures provide a pathway that can regulate the chemical exchange between the two pools and allow robust detection, especially under high pressure during the ^{129}Xe NMR/MRI experiment. Although FLAME had a similar exchange rate to cryptophane A, FLAME was much more effective because the liquid PFOB core of FLAME could accommodate 10^3–10^4 xenon atoms under standard conditions (xenon Ostwald solubility coefficient in PFOB ~1.2 and in water ~0.08 at 37 °C).[5b] Indeed, this approach was analogous to the approach of LipoCEST or CellCEST agents by Aime and colleagues, where liposomes or red blood cells were encapsulated with a large number of paramagnetic shift reagents to maximize the per-agent PARACEST contrast.[14] Furthermore, FLAME is convenient to synthesise and perform surface modification with various functional groups for targeted imaging or drug delivery.

In summary, we successfully developed a targeted FLAME-based ^{129}Xe biosensor that recognizes $\alpha_v\beta_3$ integrin with high specificity. FLAME was proven to be an excellent Hyper-CEST reporter because of the core–shell structures. FLAME could overcome the following two major limitations by coating the surface with silica: (1) the rapid chemical exchange of ^{129}Xe between the PFC nanoemulsion and solution and (2) the impractical modifiability of the surface of the nanoemulsion. After living cell NMR experiments, we demonstrated its use for targeted live-cell molecular imaging *via* Hyper-CEST MRI. The coated PFOB nanoparticles have considerable potential for further biological imaging.

Conflicts of interest

There are no conflicts to declare.

Acknowledgements

This work was supported by National Key R&D Program of China (2018YFA0704000), National Natural Science Foundation of China (91859206, 81625011), Key Research Program of Frontier Sciences, CAS (ZDBS-LY-JSC004, QYZDY-SSW-SLH018) and Hubei Provincial Natural Science Foundation of China (2017CFA013, 2018ACA143).

Notes and references

1 (*a*) Y. Wang and I. J. Dmochowski, *Acc. Chem. Res.*, 2016, **49**, 2179; (*b*) S. Klippel, J. Döpfert and J. Jayapaul, *et al.*, *Angew. Chem., Int. Ed.*, 2014, **53**, 493.

2 (*a*) M. Albert, G. Cates, B. Driehuys, W. Happer, B. Saam, C. Springer Jr and A. Wishnia, *Nature*, 1994, **370**, 199; (*b*) B. Driehuys, G. P. Cofer, J. Pollaro, J. B. Mackel, L. W. Hedlund and G. A. Johnson, *Proc. Natl. Acad. Sci. U. S. A.*, 2006, **103**, 18278; (*c*) X. Zhou, Y. Sun, M. Mazzanti, N. Henninger, J. Mansour, M. Fisher and M. Albert, *NMR Biomed.*, 2011, **24**, 170; (*d*) H. Li, Z. Zhang, X. Zhao, X. Sun, C. Ye and X. Zhou, *Magn. Reson. Med.*, 2016, **76**, 408.

3 (*a*) H. M. Rose, C. Witte, F. Rossella, S. Klippel, C. Freund and L. Schröder, *Proc. Natl. Acad. Sci. U. S. A.*, 2014, **111**, 11697; (*b*) M. Schnurr, K. Sydow, H. M. Rose, M. Dathe and L. Schröder, *Adv. Healthcare Mater.*, 2015, **4**, 40; (*c*) Q. Guo, Q. Zeng, W. Jiang, X. Zhang, Q. Luo, X. Zhang, L. S. Bouchard, M. Liu and X. Zhou, *Chem. – Eur. J.*, 2016, **22**, 3967; (*d*) B. A. Riggle, Y. Wang and I. J. Dmochowski, *J. Am. Chem. Soc.*, 2015, **137**, 5542; (*e*) Q. Zeng, Q. Guo, Y. Yuan, Y. Yang, B. Zhang and X. Zhou, *Anal. Chem.*, 2017, **89**, 2288.

4 (*a*) Y. Wang and I. J. Dmochowski, *Chem. Commun.*, 2015, **51**, 8982; (*b*) M. Kunth, C. Witte, A. Hennig and L. Schrçder, *Chem. Sci.*, 2015, **6**, 6069; (*c*) M. Schnurr, J. Sloniec-Myszk,

J. Döpfert, L. Schröder and A. Hennig, *Angew. Chem., Int. Ed.*, 2015, **54**, 13444; (*d*) Y. Wang, B. W. Roose, J. P. Philbin, J. L. Doman and I. J. Dmochowski, *Angew. Chem., Int. Ed.*, 2016, **55**, 1733; (*e*) J. A. Finbloom, C. C. Slack, C. J. Bruns, K. Jeong, D. E. Wemmer, A. Pines and M. B. Francis, *Chem. Commun.*, 2016, **52**, 3119; (*f*) C. C. Slack, J. A. Finbloom, K. Jeong, C. J. Bruns, D. E. Wemmer, A. Pines and M. B. Francis, *Chem. Commun.*, 2017, **53**, 1076; (*g*) B. Zhang, Q. Guo, Q. Luo, X. Zhang, Q. Zeng, C. Ye and X. Zhou, *Chem. Commun.*, 2018, **54**, 13654.

5 (*a*) J. Wolber, I. J. Rowland, M. O. Leach and A. Bifone, *Magn. Reson. Med.*, 1999, **41**, 442; (*b*) T. K. Stevens, R. M. Ramirez and A. Pines, *J. Am. Chem. Soc.*, 2013, **135**, 9576; (*c*) S. Klippel, C. Freund and L. Schröder, *Nano Lett.*, 2014, **14**, 5721; (*d*) H. Zhang, S. Chen, Y. Yuan, Y. Li, Z. Jiang and X. Zhou, *ACS Appl. Bio Mater.*, 2019, **2**, 27.

6 (*a*) M. G. Shapiro, R. M. Ramirez, L. J. Sperling, G. Sun, J. Sun, A. Pines, D. V. Schaffer and V. S. Bajaj, *Nat. Chem.*, 2014, **6**, 629; (*b*) M. Kunth, G. J. Lu, C. Witte, M. G. Shapiro and L. Schröder, *ACS Nano*, 2018, **12**, 10939.

7 (*a*) Y. Wang, B. W. Roose, E. J. Palovcak, V. Carnevale and I. J. Dmochowski, *Angew. Chem., Int. Ed.*, 2016, **55**, 1; (*b*) B. W. Roose, S. D. Zemerov, Y. Wang, M. A. Kasimova, V. Carnevale and I. J. Dmochowski, *Chem. Phys. Chem.*, 2019, **20**, 260.

8 (*a*) K. Bartik, M. Luhmer, J.-P. Dutasta, A. Collet and J. Reisse, *J. Am. Chem. Soc.*, 1998, **120**, 784; (*b*) M. M. Spence, S. M. Rubin, I. E. Dimitrov, E. J. Ruiz, D. E. Wemmer, A. Pines, S. Q. Yao, F. Tian and P. G. Schultz, *Proc. Natl. Acad. Sci. U. S. A.*, 2001, **98**, 10654; (*c*) L. Schröder, T. J. Lowery, C. Hilty, D. E. Wemmer and A. Pines, *Science*, 2006, **314**, 446; (*d*) G. K. Seward, Y. Bai, N. S. Khan and I. J. Dmochowski, *Chem. Sci.*, 2011, **2**, 1103.

9 P. C. Van Zijl and N. N. Yadav, *Magn. Reson. Med.*, 2011, **65**, 927.

10 (*a*) H. Matsushita, S. Mizukami, F. Sugihara, Y. Nakanishi, Y. Yoshioka and K. Kikuchi, *Angew. Chem., Int. Ed.*, 2014, **53**, 1008; (*b*) T. Nakamura, F. Sugihara, H. Matsushita, Y. Yoshioka, S. Mizukamiab and K. Kikuchi, *Chem. Sci.*, 2015, **6**, 1986; (*c*) T. Nakamura, H. Matsushita, F. Sugihara, Y. Yoshioka, S. Mizukami and K. Kikuchi, *Angew. Chem., Int. Ed.*, 2015, **54**, 1007; (*d*) R. Narayan, U. Y. Nayak, A. M. Raichur and S. Garg, *Pharmaceutics*, 2018, **10**, 118; (*e*) Q. Qu, Y. Si and H. Xuan, *et al.*, *Mater. Lett.*, 2018, **211**, 40; (*f*) I. I. Slowing and L. Juan, *et al.*, *Adv. Drug Delivery Rev.*, 2008, **60**, 1278.

11 (*a*) P. S. Winkel, C. J. Glinka and G. D. Stucky, *Langmuir*, 2000, **16**, 356; (*b*) Z. Teng, Y. Han, J. Li, F. Yan and W. Yang, *Microporous Mesoporous Mater.*, 2010, **127**, 67.

12 (*a*) M. Zaiss, M. Schnurr and P. Bachert, *J. Chem. Phys.*, 2012, **136**, 144106; (*b*) M. Kunth, C. Witte and L. Schröder, *J. Chem. Phys.*, 2014, **141**, 194202.

13 (*a*) A. D. Corso, L. Pignataro, L. Belvisi and C. Gennari, *Curr. Top. Med. Chem.*, 2016, **16**, 314; (*b*) A. Taherian, X. Li, Y. Liu and T. A. Haas, *BMC Cancer*, 2011, **11**, 293; (*c*) C. Chetty, S. S. Lakka, P. Bhoopathi and J. S. Rao, *Int. J. Cancer*, 2010, **127**, 1081.

14 (*a*) S. Aime, C. Carrera, D. Delli Castelli, S. Geninatti Crich and E. Terreno, *Angew. Chem., Int. Ed.*, 2005, **44**, 1813; (*b*) S. Aime, D. Delli. Castelli and E. Terrenoi, *Angew. Chem., Int. Ed.*, 2005, **44**, 5513; (*c*) S. Aime, D. D. Castelli and E. Terrenoi, *Angew. Chem., Int. Ed.*, 2007, **46**, 966; (*d*) G. Ferrauto, E. D. Gregorio, S. Baroni and S. Aime, *Nano Lett.*, 2014, **14**, 6857.

